electronics

Article

Expanding Imaging of Satellites in Space (IoSiS): A Feasibility Study on the 3-Dimensional Imaging of Satellites Using Interferometry and Tomography

Fabian Hochberg *, Matthias Jirousek, Simon Anger and Markus Peichl

German Aerospace Center (DLR), Microwaves and Radar Institute, Muenchenerstrasse 20, 82234 Wessling, Germany
* Correspondence: fabian.hochberg@dlr.de

Abstract: As the need for new and advanced space situational awareness systems increases, new technologies for in situ observations are needed. The experimental IoSiS (Imaging of Satellites in Space) system at the German Aerospace Center (DLR) is already capable of high-resolution imaging tasks using inverse synthetic aperture radar technology. As two-dimensional radar images can be difficult to interpret, full three-dimensional imaging is desired. This paper extends the previously published simulation aspects to real ground-based experiments using a single spatially separated receiver, allowing interferometric measurements. However, as interferometry cannot fully resolve a three-dimensional object, more spatially separated receivers are also considered for the use of ISAR tomography to gain experimental insight into true three-dimensional imaging as IoSiS will eventually move toward a tomographic acquisition mode. The results shown here promise a high-resolution imaging method for the future development of IoSiS. Based on the research presented here, additional receivers can be implemented into IoSiS to establish real-world three-dimensional measurements of space objects.

Keywords: inverse synthetic aperture radar (ISAR); satellite imaging; SAR interferometry; ISAR tomography; space surveillance

Citation: Hochberg, F.; Jirousek, M.; Anger, S.; Peichl, M. Expanding Imaging of Satellites in Space (IoSiS): A Feasibility Study on the 3-Dimensional Imaging of Satellites Using Interferometry and Tomography. *Electronics* **2024**, *13*, 4914. https://doi.org/10.3390/electronics13244914

Academic Editor: Paul Mitchell

Received: 13 November 2024
Revised: 4 December 2024
Accepted: 10 December 2024
Published: 12 December 2024

1. Introduction

In recent history, many more parties have gained affordable access to space. Numerous spacecraft and the resulting space debris are entering Earth's orbit, which has consequently created the demand for new and advanced space situational awareness (SSA) systems. The German Aerospace Center (DLR) built an experimental radar system called IoSiS (Imaging of Satellites in Space) for high-resolution with in situ imaging based on the concept of inverse synthetic aperture radar (ISAR) [1].

Imaging radar systems such as IoSiS produce two-dimensional images that can be difficult to interpret due to geometric distortions. In addition, complex objects such as satellites are simply not well described by a two-dimensional image. To contribute to global SSA and to provide satellite operators with more information, a three-dimensional imaging system is desired. This paper explores the concept of interferometry and tomography to extend the capability of IoSiS to deliver three-dimensional image products.

Three-dimensional imaging using imaging radar technology relies on the coherent integration of the radar echo signal received from many observation angles. In the context of IoSiS, this can be achieved by using additional spatially separated receivers that receive the radar echo at spatially distributed positions. The principle of IoSiS can be seen in Figure 1, where a secondary receiving (RX) antenna in blue denotes the new proposed receiver for interferometry. The new look angle on the satellite allows the use of interferometry for a quasi-three-dimensional image. Further developments toward true three-dimensional imaging through the concept of ISAR tomography can be established by adding more and

more receivers to create a secondary aperture to achieve a proper resolution in all three spatial dimensions. This is represented by the receiver units coloured in green in Figure 1.

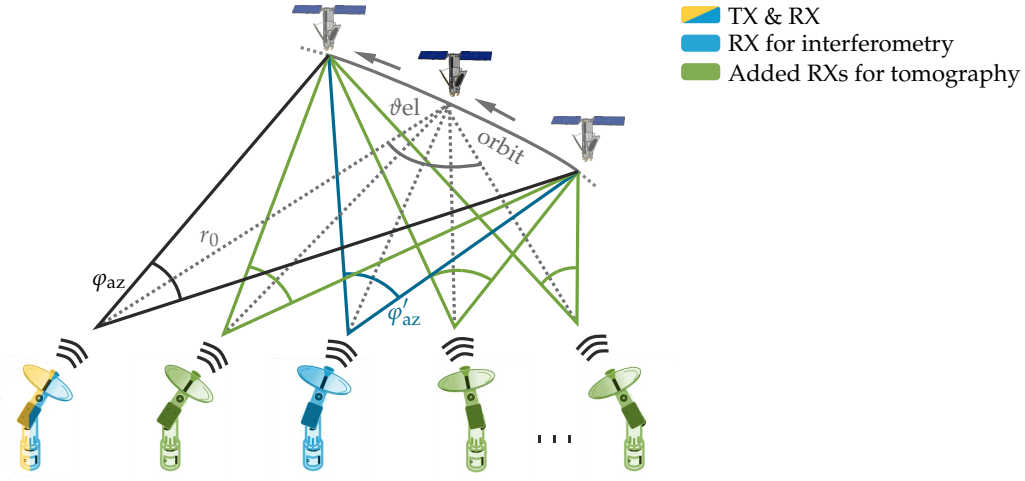

Figure 1. The working principle of IoSiS and the proposed spatially separated receiver in blue for interferometry. The additional receivers needed for tomography are denoted in green.

Other works such as [2] have already shown a few experimental results for a similar type of radar in a ground-based setup, focusing on object reconstruction based on wide-angle interferometric measurements. In addition, object characterisation using simulated datasets has been investigated in [3]. However, this work embeds the interferometric and tomographic imaging concept within IoSiS and analyzes the feasibility of using the new digital interface for IoSiS, currently in development, in a ground-based manner. Thus, it extends the previously published simulation studies for the IoSiS three-dimensional imaging approach and compares the imaging results obtained using interferometric and tomographic measurements. Furthermore, the first exemplary application in the form of change detection is shown.

This paper is structured as follows: Section 2 introduces the theoretical imaging principle in the context of IoSiS, firstly in terms of interferometry (Section 2.1), secondly in terms of tomography (Section 2.2), and finally in terms of the unique geometric considerations applicable to IoSiS (Section 2.3). Next, Section 3 introduces the new digital radar interface currently being developed for IoSiS and explains the experimental radar setup used to obtain the ground-based experimental results shown in this paper. The measurement results are then presented and analyzed in Section 4, before a summary and outlook for IoSiS is given in Section 5.

2. Radar Theory for 3-Dimensional Imaging

In order to extend IoSiS's capabilities into the realm of three-dimensional imaging, the concept of interferometry can be used. By comparing the phase difference between two ISAR acquisitions on a per-pixel basis, the third spatial dimension can be observed.

IoSiS uses a chirp pulse radar to allow high-resolution acquisition over the large distances from the radar to the satellite. With the next generation of IoSiS, the goal is to use up to 4.4 GHz of bandwidth for a theoretical range resolution of 3.4 cm. Many SAR or ISAR algorithms have been developed and investigated [4]. For more complex platform trajectories (or in the case of IoSiS, object trajectories), the back-projection algorithm is widely used and is also applied in the context of IoSiS [1]. This algorithm uses knowledge about the imaging geometry to coherently project the radar data onto a focal plane.

Certainly, a satellite passing above the observation site exhibits heavily time-varying changes in distance and orientation. For a good focus, not only the orbit but also the attitude needs to be known or estimated using motion-compensation algorithms, like [5–7].

However, operational satellites usually have active attitude control. This implies that the alteration in the disposition of these satellites can be predicted solely on the basis of their orbital parameters. This has been demonstrated by the IoSiS system, which does not necessitate the utilization of sophisticated compensation algorithms for the imaging of non-cooperative satellites in operation. In the case of imaging space objects that lack active attitude control (such as defective satellites or space debris), more sophisticated focusing algorithms are required. However, this is beyond the scope of the present paper.

The image generation in the two-dimensional case can be seen in Equation (1), where $s(\boldsymbol{r'})$ is the complex radar image at the pixel location $\boldsymbol{r'}$. The measurement data are represented by $h(\Delta r, \varphi)$ and depend on the relative range toward the pixel at $\boldsymbol{r'}$ and the azimuth integration angle φ along the satellite's orbit. The exponential phase-correction term is used to shift the data back to the correct central spatial frequency p_c using the central frequency f_c and the correct image central distance r_0. The total integration angle is denoted by φ_{az} and can also be geometrically found in Figure 1. The integration angle φ_{az} for the main receiver and φ'_{az} for the secondary receiver around the central look angle φ_c can be assumed to be the same.

$$s(\boldsymbol{r'}) = \sum_{\varphi_c - \frac{\varphi_{az}}{2}}^{\varphi_c + \frac{\varphi_{az}}{2}} h(\Delta r, \varphi) \cdot e^{j p_c (r_0 - \Delta r)} \quad \text{with} \quad p_c = \frac{4\pi f_c}{c_0}, \quad \Delta r = \|\boldsymbol{r'} - \boldsymbol{r_0}\| \quad \text{and} \quad r_0 = \|\boldsymbol{r_0}\| \tag{1}$$

2.1. Quasi-3-Dimensional Imaging by Interferometry

After the well-known regular ISAR image acquisition, the first extension toward the three-dimensional acquisition mode can be established. Interferometry in the context of SAR has been established for many years [8]. By obtaining an SAR acquisition from two or more different positions, an interferogram v can be computed by Equation (2), where the vector $\boldsymbol{r'}$ points to a specific point on the imaging plane and s_1 and s_2 are the two different SAR or ISAR acquisitions, respectively.

$$v(\boldsymbol{r'}) = s_1(\boldsymbol{r'}) \cdot s_2^*(\boldsymbol{r'}) \tag{2}$$

As the imaging geometry is already known to the processing algorithm to a high degree of accuracy, the process of coregistration the two acquisitions for interferogram generation should be accomplishable with well-known methods. From the phase difference of the pixel at $\boldsymbol{r'}$, the path length difference Δr can be computed, which in turn allows the computation of the height offset from the imaging plane. This can be seen in Equations (3) and (4), where λ_c is the wavelength at the radar's center frequency, r_c is the median distance from the scenery, and $b_\perp$ is the baseline length connecting the sensors, projected to the normal direction of the imaging plane.

$$\Delta r = \frac{\angle v(\boldsymbol{r'})}{2\pi} \cdot \lambda_c \tag{3}$$

$$\Delta z = \frac{r_c}{\sqrt{b_\perp^2 - \Delta r^2}} \cdot \Delta r \tag{4}$$

It should be mentioned that any phase measurement is 2π-ambiguous. That also means that for a given acquisition, large offsets Δz toward the focal plane would have a phase offset greater than 2π, which cannot be inferred directly from measurements. This is fundamental to all interferometric SAR acquisitions, and therefore, phase unwrapping algorithms have been developed in the context of Earth observation [9]. However, as IoSiS images complex objects without any a priori information, and phase unwrapping cannot be performed. This is a fundamental effect in interferometric SAR measurements and needs to be investigated carefully. As it is closely related to the imaging geometry, this issue is examined in more detail in Section 2.3.

However, as the two images are obtained from different observation angles, a loss of coherence is to be expected. The interferometric correlation coefficient can be described by

Equation (5) [8], where $\mathrm{E}\{\cdot\}$ is the expectation operator and $\circ$ is the Hadamard product for an element-wise product of the ISAR images s_1 and s_2, respectively. When imaging complex objects against a reflection free background (space), there will be image regions containing no information. This results in a low coherence between the images in those regions, which also renders the interferometric phase meaningless. The application of interferometric evaluation is only feasible in regions of high coherence. The coherence image, which is formed over small image areas by applying Equation (5), can be used with a simple threshold filter to mask the interferometric phase evaluation to areas of interest. The threshold mask definition can be seen in Equation (6), where the threshold γ_{thr} is the coherence cut-off and $-$ denotes that the pixel at $\boldsymbol{r'}$ is omitted from further evaluation, resulting in the masked interferogram v_{thr}.

$$\gamma = \frac{\mathrm{E}\{s_1 \circ s_2^*\}}{\sqrt{\{|\mathrm{s}_1|^2\} \cdot \{|\mathrm{s}_2|^2\}}} \qquad \text{where} \quad \gamma \in [0,1] \tag{5}$$

$$v_{\mathrm{thr}}(\boldsymbol{r'}) = \begin{cases} v(\boldsymbol{r'}) & \text{if } \gamma(\boldsymbol{r'}) \geq \gamma_{\mathrm{thr}} \\ - & \text{if } \gamma(\boldsymbol{r'}) < \gamma_{\mathrm{thr}} \end{cases} \tag{6}$$

Layover Effect Mitigation in Interferometric Measurements

Furthermore, another significant phenomenon in all SAR acquisitions that can be addressed in the context of interferometry is the so-called foreshortening or layover effect [10]. This arises due to the imaging geometry, whereby off-focus scatterers are projected onto pixels at the same distance from the radar as the scatterer, thereby distorting their position in the radar image. In the case of satellite imaging, where the reconstruction of a singular object by strong scatterers is desired, interferometric measurements allow the mitigation of this effect. The cause of this effect is the elevated incidence angle on the focal plane, which changes the observed range from a scatterer outside the focal plane as can be seen in Figure 2. In combination with the a priori knowledge of the imaging geometry, this allows the correction to be done by Equation (7), where Δx is the correction needed along the mean look angle in the azimuth and θ is the incidence angle from the radar normal to the focal plane. A simulation example is shown in Figure 3, where the experimental ground-based radar setup, which is described in more detail in Section 3, is simulated to demonstrate the correction capability. Figure 3a shows the simulated ISAR image and the 32 automatically detected targets. Assigning each target a height through its interferometric phase results in the light red dots in 3D space in Figure 3b. As can be clearly seen, the three-dimensional reconstruction is not carried out correctly, as the dots do not align with the true positions denoted with the blue dots. Applying the correction from (7) shifts the targets toward their true position as seen in Figure 3c. It should be noted that this is only an approximation for small integration angles. If the integration angle is large, the scatterers will defocus and show an angle-dependent offset from the true position. For very high integration angles and/or large offsets from the focal plane, the scatterer will smear and not focus correctly [11]. The correction capability is ultimately limited by the target detection algorithm, which extracts the point cloud of the imaged object.

$$\Delta x = \frac{\Delta z}{\tan\theta} \tag{7}$$

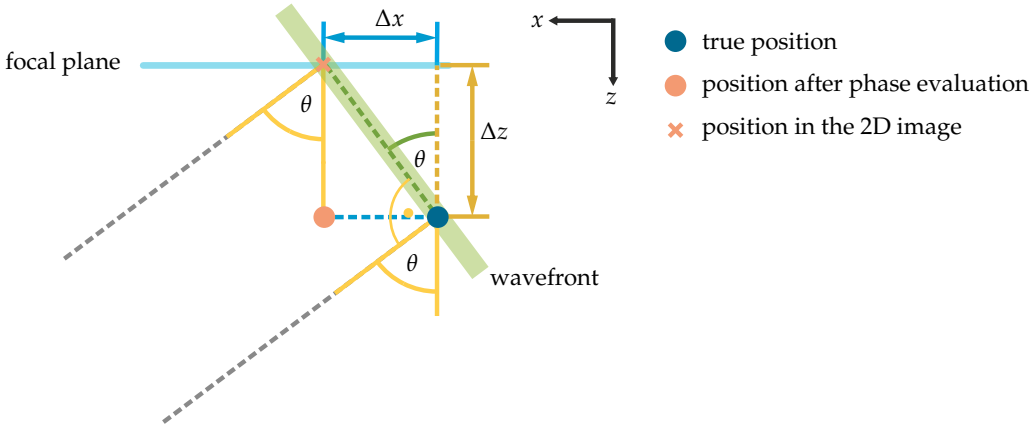

Figure 2. Geometric visualization of the layover effect and the correction geometry under the approximation of a small integration angle.

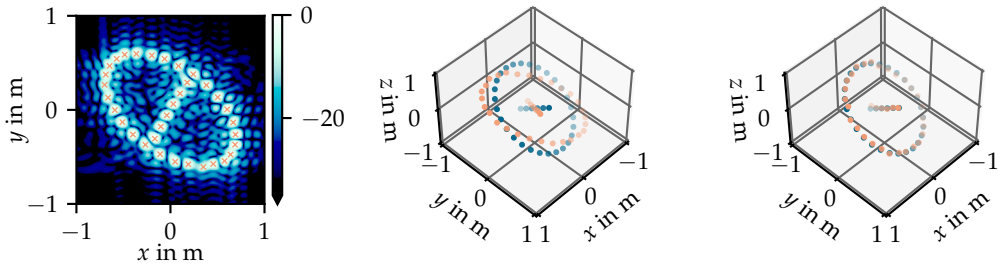

(**a**) (**b**) (**c**)

Figure 3. Simulative demonstration of the layover effect and the proposed correction to generate a 3D point cloud based on an interferometric acquisition. (**a**) Simulated ISAR image for a 3-dimensional distribution of ideal targets. The targets are automatically detected and marked with a cross in light red. The color represents the normalized amplitude in dB. (**b**) Three-dimensional extraction of the simulated scenario. The true positions are marked in blue, whereas the positions extracted using only the interferometric phase are represented in light red. (**c**) Three-dimensional extraction of the simulated scenario. The true positions are marked in blue, whereas the positions extracted using the interferometric phase and the correction from Equation (7) are represented in light red.

2.2. True 3-Dimensional Imaging by Tomography

However, interferometry is only capable of assigning each pixel an offset from the imaging plane, thereby displaying a kind of topography. It is not possible to separate multiple scatterers aligned along the normal direction of the imaging plane using interferometry. In order to achieve true three-dimensional imaging of satellites, a tomographic imaging acquisition is required. In order to facilitate this, a multitude of receivers will need to be added to IoSiS in order to span a secondary aperture. This principle has already been shown in [12] and thus is not shown in exhaustive detail here. In short, extending the image generation from Equation (1) to a tomographic imaging geometry adds a secondary summation form $\vartheta_c - \frac{\vartheta_{el}}{2}$ to $\vartheta_c + \frac{\vartheta_{el}}{2}$ and expands the measurement space to $h(\Delta r, \varphi, \vartheta)$. The central look angle in elevation is denoted by ϑ_c and the look angle under which the satellite is observed ϑ_{el} can be found in Figure 1. This can be seen in Equation (8), where the vector $\boldsymbol{r}'$ is now pointing to all 3-dimensional image pixels.

In particular, the imaging volume must be fixed in relation to the moving satellite and must rotate in accordance with the satellite's attitude, as is the case in two-dimensional imaging. As previously stated, strong regularity in the operational satellites' attitude is observed and can be determined based on the orbit geometry.

$$s(\boldsymbol{r'}) = \sum_{\vartheta_c - \frac{\vartheta_{el}}{2}}^{\vartheta_c + \frac{\vartheta_{el}}{2}} \sum_{\varphi_c - \frac{\varphi_{az}}{2}}^{\varphi_c + \frac{\varphi_{az}}{2}} h(\Delta r, \varphi, \vartheta) \cdot e^{j p_c (r_0 - \Delta r)}$$
$$\text{with} \quad p_c = \frac{4\pi f_c}{c_0}, \quad \Delta r = \|\boldsymbol{r'} - \boldsymbol{r_0}\| \quad \text{and} \quad r_0 = \|\boldsymbol{r_0}\| \tag{8}$$

2.3. Geometric Considerations

The quality of ISAR measurements is highly influenced by the imaging geometry used for data acquisitions. Resolution and ambiguity suppression are the key factors in choosing the position of the secondary receiver or the receiving array.

Regarding interferometry, the physical placement of the secondary receiving antenna is of utmost importance, as it defines the height of ambiguity. The height of ambiguity is the region around the focal plane where an unambiguous mapping from phase to height is possible before a phase jump occurs. Moreover, the height of ambiguity is dependent on the orbit height h_{sat}, the central wavelength λ_c, and the perpendicular distance between the antennas $b_\perp$, as seen in Equation (9), which is only valid for a satellite passing through the zenith of the observation site.

$$h_{amb} = \frac{\lambda_c h_{sat}}{b_\perp} \tag{9}$$

In Figure 4, this relationship can be seen. In combination with the phase resolution of the radar system, a quasi-resolution in z-direction, which is perpendicular to the focal plane, can be defined by Equation (10), where h_{amb} is the height of ambiguity and σ_φ is the phase accuracy of the radar.

$$\delta_z = \frac{h_{amb}}{2\pi} \cdot \sigma_\varphi \tag{10}$$

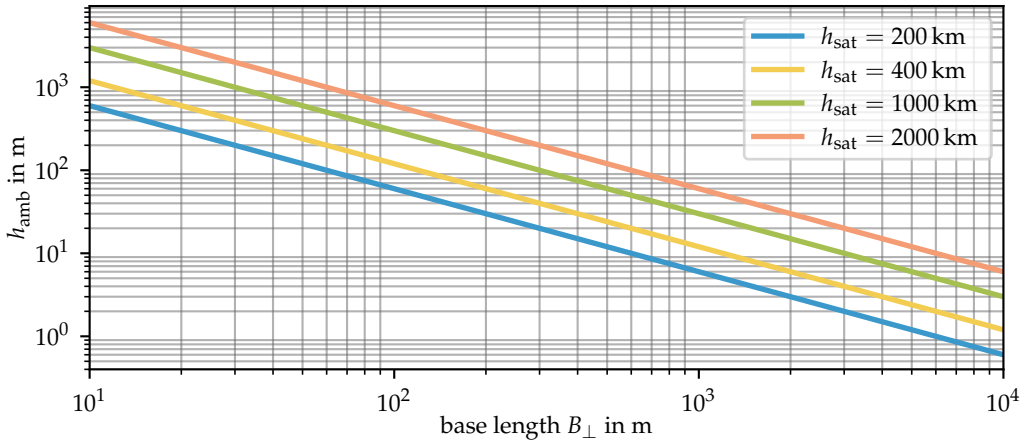

Figure 4. Relationship for the height of ambiguity for different orbit heights for a central frequency of $f_c = 10$ GHz.

For high resolution and many resolution cells in the z-direction, a highly stable radar system needs to be used, which allows fine phase measurements. As already stated in Section 2.1, phase unwrapping cannot be performed. To ideally make use of the ambiguous-free space, the antennas should be as far apart as possible to just fit the expected satellite into a single height of ambiguity. This would maximize the interferometric resolution, as the complete ambiguity-free height can be used. Taking a look at the mass distribution of satellites in space in Figure 5, it can be clearly seen that most satellites are around 0.25 t to 0.5 t. These data allow an indirect size estimation, because geometric considerations of objects' actual sizes are not publicly available for many satellites. For example, the TerraSAR-X satellite is about 4.9 m × 2.4 m × 2.4 m large and has a launch

mass of about 1.2 t [13], meaning most satellites are probably smaller than or equal to that. Depending on the satellites' configuration, some foldable elements (e.g., solar panels) may be present, which renders physical size estimation based on launch mass challenging. On the contrary, the International Space Station (ISS) is an exceptionally large and heavy object with just shy of 420 t and a size of about 109 m × 73 m × 51 m [14]. Being able to observe the ISS would be much desired as it is a complex structure with many features. And it is thus the ideal test target for an experimental system such as IoSiS. However, configuring the imaging geometry for the ISS as the expected object would result in a lower resolution for practically all other objects. Thus, a flexible secondary receive antenna would be ideal, which is also why IoSiS first spatially separated receiver will be a flexible positionable device.

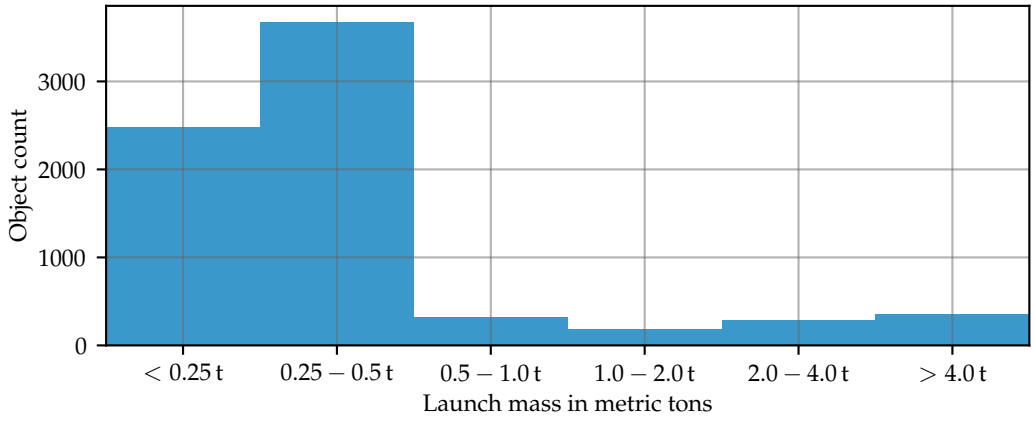

Figure 5. Distribution of satellites' launch masses currently in orbit. The data plot is based on the database from [15].

Until now, only the distance between the antennas has been considered. In reality, the true relative positions in relation to the orbits' path are important as the imaging plane lies along the orbit path. Thus, the z-direction perpendicular to the imaging plane changes from satellite pass to satellite pass. To illustrate this fact, two exemplary satellite passes and a stationary positioning of a secondary receive antenna can be seen in Figure 6a,b. As can clearly be seen here, a flexible positionable receiving antenna would again be ideal.

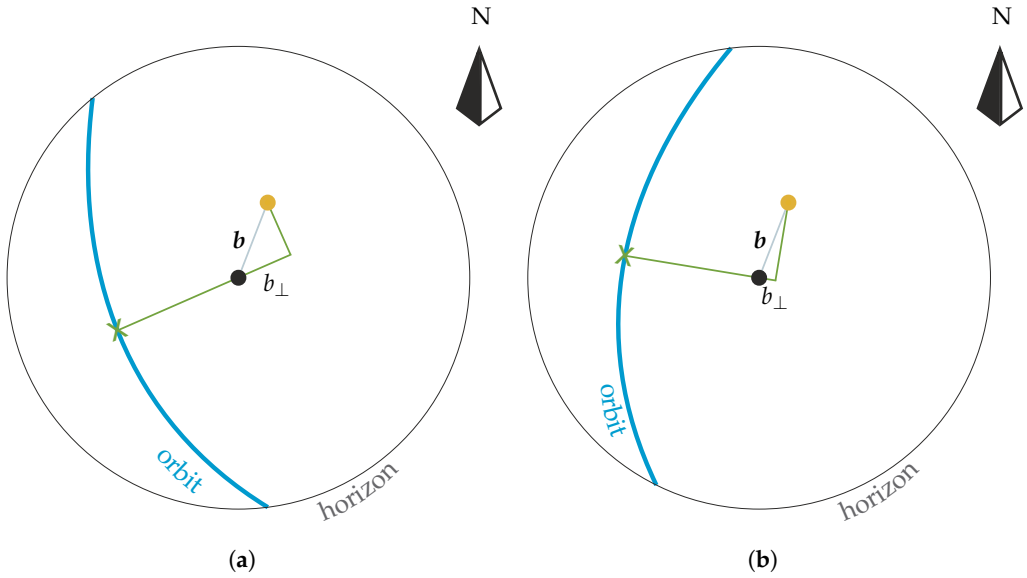

Figure 6. *Cont.*

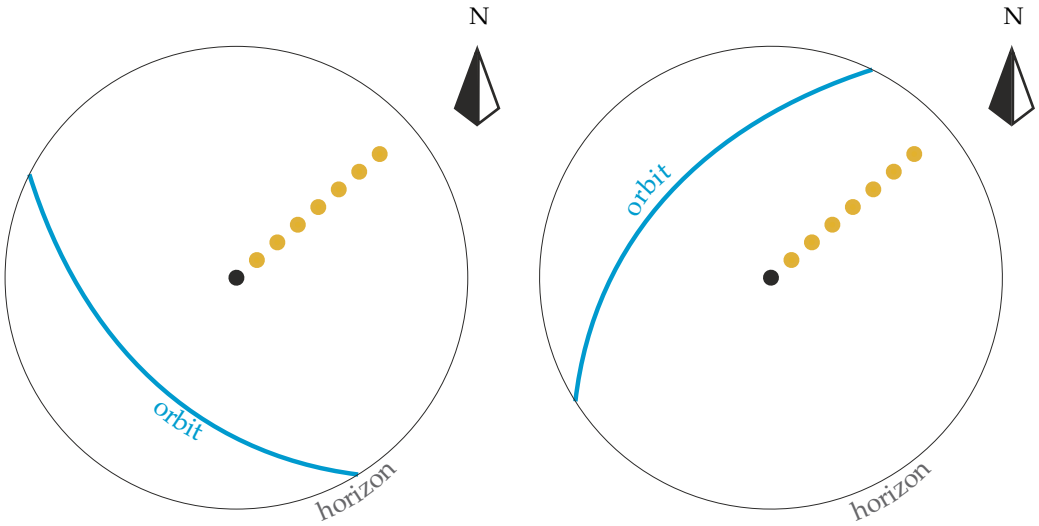

Figure 6. A few exemplary antenna arrangements in a projected view. The main TX and RX antenna is represented by the black dot, and the orange dots represent the secondary receiving antennas. (**a**) An exemplary antenna arrangement for interferometric measurements. The green cross represents the point of closest approach, where the interferometric baseline $b_\perp$ is taken. (**b**) The same antenna arrangement as in (**a**), but with a different satellite pass as an example. The baseline $b_\perp$ is considerably smaller. (**c**) An exemplary antenna arrangement for tomographic measurements. The orbit path has only a little component along the array track, which samples the echo signal in elevation very well. (**d**) The same antenna arrangement as in (**c**), but with a different satellite pass as an example. Here, the orbit path aligns with the array line and thus significantly reduces the possible resolution.

Regarding the tomographic imaging of satellites, many more receivers need to be used to give multiple viewing angles. The angle ϑ_{el} under which the satellite is observed defines, in combination with the satellites' height h_{sat} and the center wavelength λ_{c}, the resolution, whereas the sampling interval defines the ambiguity suppression [16]. The placement will only be briefly touched on here as it is currently the subject of more detailed research. The simplest form of placement would be a linear array perpendicular to the orbit's path. But this would require numerous receivers to ideally sample the spatial frequency domain. Additionally, a linear array would perform well for a specific orbit path but poorly for another, which is also illustrated in Figure 6c and Figure 6d, respectively. An orbit passing directly over the array would be an even more optimal scenario than that depicted in Figure 6c, but is not shown for simplicity. A compromise between flexibility regarding the orbit, resolution and ambiguity supersession must be found and analyzed in more detail in the future, possibly using the concept of compressed sensing to reduce the number of receivers needed [17].

3. Experimental Setup Using the New Multichannel FPGA Unit

The current radar system used for IoSiS, called GigaRad, will need to be upgraded to allow three-dimensional measurements for IoSiS. As multi-static radar acquisitions have very stringent timing requirements, the digital interfaces of GigaRad will need replacement. The waveform generation, signal acquisition, and timing are currently performed by separate devices. With the rise of high performance field-programmable gate arrays (FPGAs) and System-on-a-Chip (SoC) platforms, waveform generation, signal acquisition, and timing can be performed on a single SoC for each spatial unit. In order to demonstrate and test the feasibility of such an SoC for a high-resolution radar, as well as to gain first insights on interferometric and real three-dimensional measurements on complex objects, a ground-based system based on an FPGA was developed.

The digital unit is based on a Zynq UltraScale+ RFSoC by AMD, which has a direct interface to sample or output the baseband signal. The unit is equipped with a high-grade clock source to allow for the tight timing needed for a multi-static system. The synchronization of multiple SoC platforms is outside the scope of this work and will be investigated further in the future. An overview of the data flow diagram can be seen in Figure 7, where the FPGA side is colored in blue and the embedded Linux operating system running a multithreaded C application is shown in yellow. Multithreading is used to handle the incoming network commands as well as the data handover from the FPGA to the non-volatile memory in the form of a solid-state drive (SSD). The user interface and the control signals with the motor controllers are implemented via a network protocol. With the configuration transmitted to the control logic, placed on the FPGA, the FPGA handles timing, transmission, and sampling. Once the trigger pulse for transmission is generated, the digital-to-analog converter (DAC) outputs the stored waveform, and two high-speed analog-to-digital converters (ADCs) sample the echo signal with a sample rate of 4.9 GSPS, allowing a theoretical single channel bandwidth of 2.45 GHz. The waveform used is an up-chirp with a 1 µs duration occupying a bandwidth of 2.1 GHz allowing for a theoretical range resolution of 7.1 cm. In this setup, all analogue channels are connected to a single sideband mixer and an antenna, which are separated to generate the bistatic measurement. The analogue mixing stages, which are visualized in the block diagram in Figure 8, are supplied with the same local oscillator (LO) signal to operate the radar system in the X-band. This radar setup can be seen in Figure 9b. For IoSiS, where each spatial unit will be equipped with its own FPGA unit, the full bandwidth with the use of I/Q mixers will be available. The baseband samples are stored on a buffer memory accessible from the FPGA, as well as from the processing side of the device, where the data handover to an SSD is carried out. Data calibration, processing, and visualization are carried out in Python 3.11.

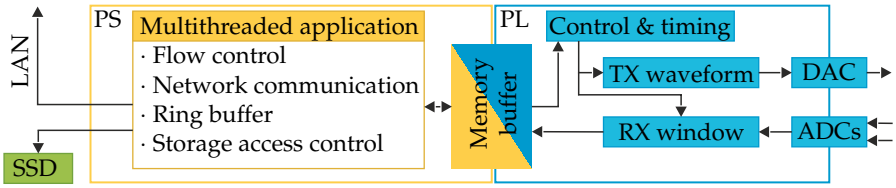

Figure 7. Basic block diagram of the developed SoC radar system with the processing system (PS) running an embedded Linux operating system in yellow and the programmable logic (PL) in blue.

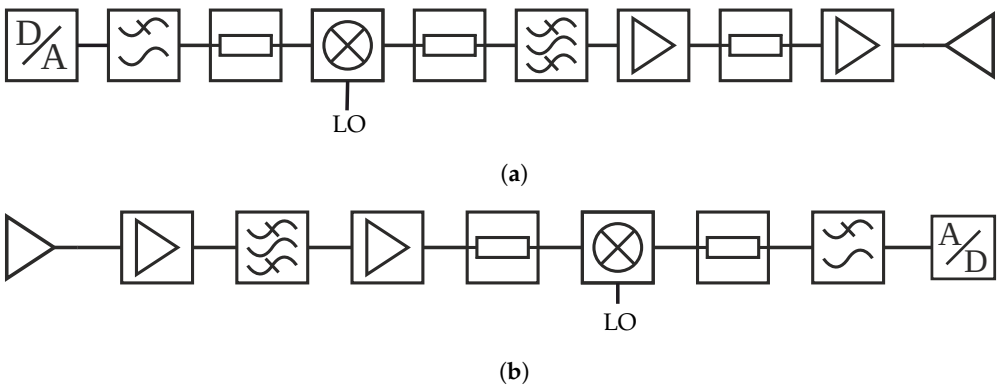

Figure 8. Block diagram of the analogue front end using the transmitter in (**a**) and the receiver in (**b**). All mixing stages are supplied with the same LO signal, the ADC is denoted with A/D and the DAC is denoted with D/A. The receiver chain is set up twice for bistatic operation.

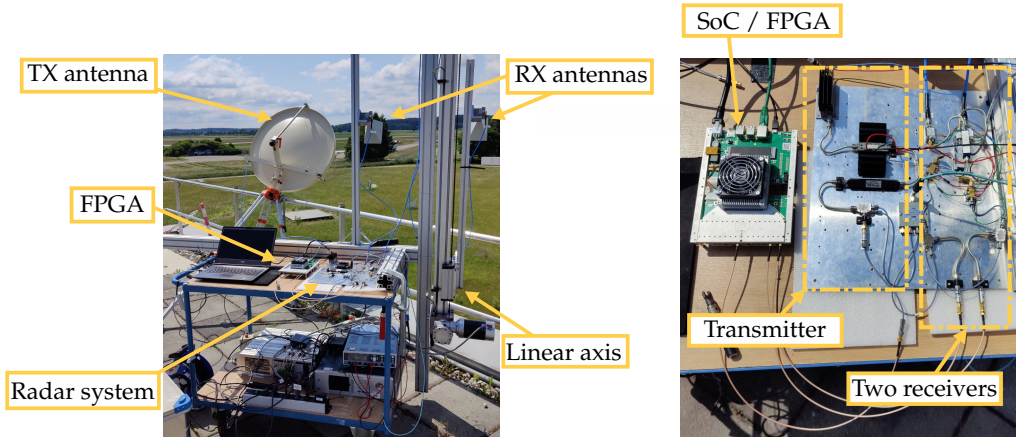

(**a**) (**b**)

Figure 9. Photos of the experimental radar setup. (**a**) Radar system in the measurement setup. (**b**) FPGA-based radar system.

4. Ground-Based Radar Measurements

Subsequently, in order to provide experimental validation of the theoretical working principle, the aforementioned two-channel radar system was constructed. All measurements were performed in a tower–turntable arrangement. This has the added benefit that all measurements are perfectly reproducible to compare the interferometric measurements of different baselines and create tomographic acquisitions by sequentially sampling all required antenna positions. A photo of the measurement setup can be seen in Figure 9a.

4.1. Idealized Demonstration Measurement

The initial experiment was a performance test utilizing the scenery depicted in Figure 10, which displays ten highly reflective targets at four distinct elevations above the turntable. The ISAR image was focused on the turntable plane, enabling interferometric height estimation. A height estimation performed by evaluating the phase at the image peaks can be used to infer the scatterers' height above the focal plane. To select the correct pixel for phase evaluation, a modified version of a CFAR algorithm was used [18]. As stated in "Section Layover Effect Mitigation in Interferometric Measurements", the layover effect can be compensated in this case.

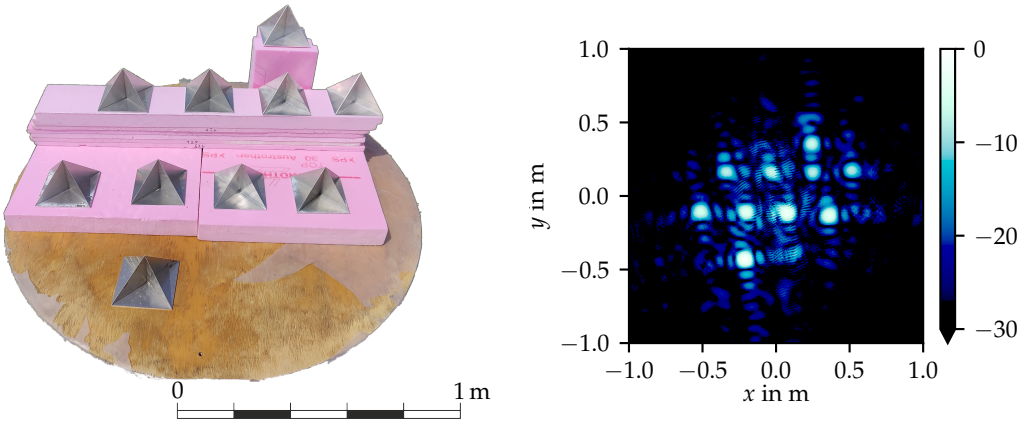

(**a**) (**b**)

Figure 10. *Cont.*

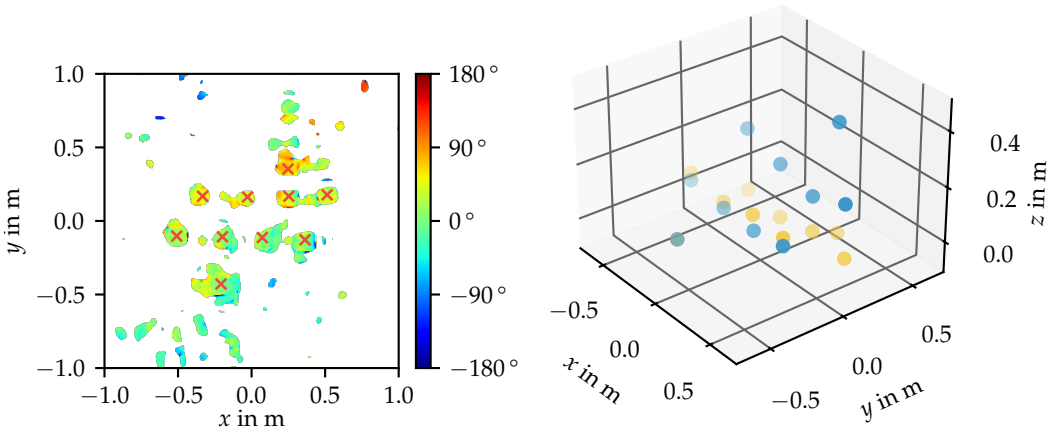

(**c**) (**d**)

Figure 10. Initial test scenery using corner reflectors at different heights to evaluate the interferometric imaging performance. (**a**) A photo of the test scenery with idealized targets. (**b**) ISAR image of the scenery in (**a**). The focal plane coincides with the turntable; the color represents the relative amplitude in dB. (**c**) Interferogram obtained by the acquisition using a base length of 21 cm and limited to a coherence of $\gamma \geq 0.85$. The red crosses show the automatically detected point-like targets; the color represents the extracted interferometric phase in degrees. (**d**) The 3-dimensional extracted scenery. The blue dots are extracted using a base length of 21 cm and the yellow dots using 77 cm.

The interferogram is shown in Figure 10c, where the automatically detected targets are marked in red. The acquisition was performed using a base length of 21 cm with a center distance of $r_0 = 23.4$ m and an incidence angle of $\theta = 59.5°$, resulting in an ambiguous-free space of 1.32 m around the focal plane. Using this geometry, both the scenario shown here and the mock-up satellite from Section 4.2 fit within the height of ambiguity. The extracted points are shown in blue in Figure 10d. One notable fact is that the four scatters at the same height are not properly on the same interferometrically inferred height. This issue arises from the fact that their side lobes interfere with each other. Using well-known side lobe suppression techniques, this effect can be greatly reduced [4]. To emphasize this fact, a Hamming window was applied in the range and the azimuth in order to suppress side lobes [19]. Table 1 illustrates the 1-σ deviation based on the four targets at the same height and their true height. It can be observed that side lobe suppression enhances the accuracy by reducing the relative height error to less than 1.7 % for both levels. Most notably, the precision is increased by a factor of approximately 1.5, which demonstrates the efficacy of the side lobe suppression technique.

In Figure 10d the result of a second interferometric acquisition is evaluated and depicted in yellow. The base length is increased to 77 cm, thus decreasing the height of ambiguity to only 36 cm, which purposefully does not fit the represented structure. As can be clearly seen, the yellow dots do not represent the measured structure correctly. The targets with higher offsets from the imaging plane are mapped to the wrong height. That is because the increased base length decreases the height of ambiguity such that the measured structure is too large to fit into a single height of ambiguity, and a phase jump occurs. This emphasizes the importance of the imaging geometry.

Table 1. True height in comparison with the interferometrically inferred height for different windows based on the measurement shown in Figure 10 with a base length of 21 cm.

True Height	Mean Interferometrically Inferred Height Rectangular/Hamming	1-σ Height Deviation Rectangular/Hamming
6 cm	5.83 cm / 6.05 cm	1.42 cm / 0.95 cm
24 cm	20.4 cm / 23.6 cm	4.04 cm / 2.29 cm

4.2. Interferometric Demonstration Measurement Using a Mock-Up Satellite

Therefore, as real satellites are more complex than the idealized scenario described in Section 4.1, the mock-up satellite depicted in Figure 11a was set up on the turntable. The satellite structure is made up of a metal frame encased in gold foil to mimic the thermal insulation of most satellites. On the right-hand side of the model, a mock-up solar panel is constructed from polystyrene with the addition of metal strips. The reflection characteristics give a reasonable approximation of the characteristics of real solar panels, as seen with the IoSiS system. To provide more three-dimensional features to the mock-up measurements to demonstrate three-dimensional imaging, an extension arm and a reflector antenna were added.

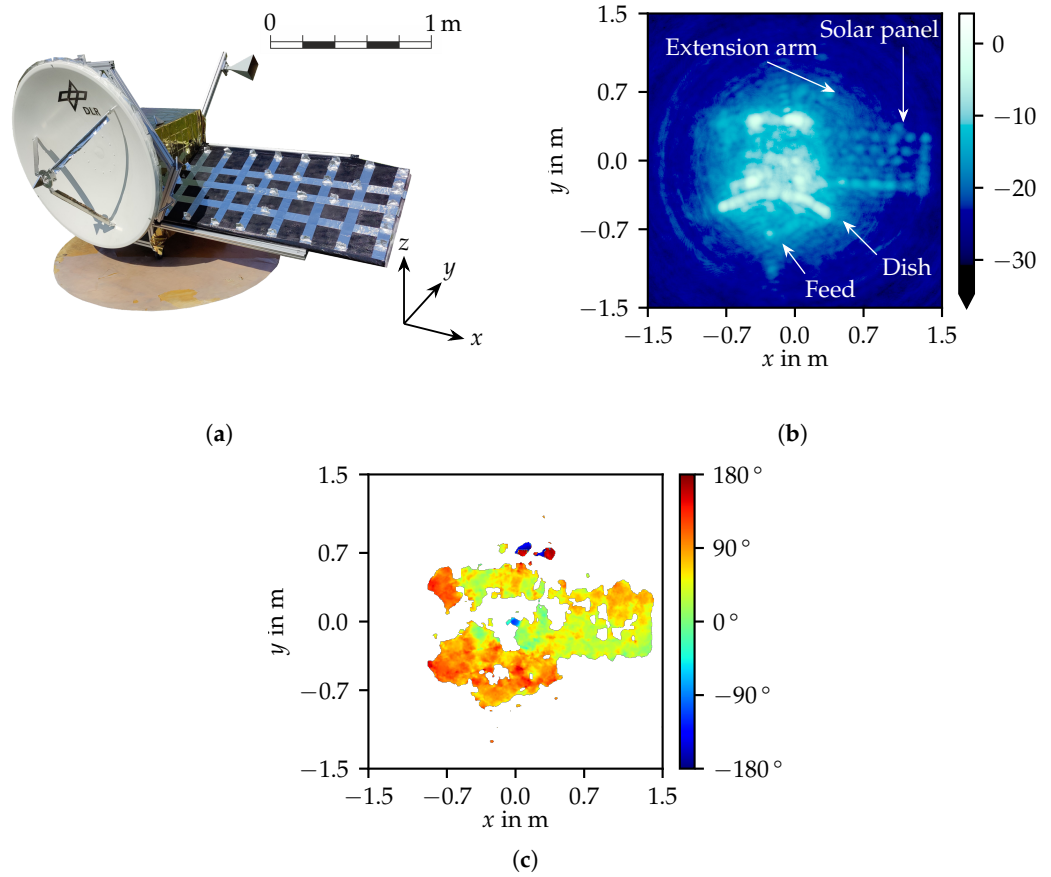

Figure 11. Mock-up satellite and corresponding interferometric ISAR measurement. (**a**) Photo of the mock-up satellite; the z-axis of the coordinate system aligns with the axis of rotation of the turntable, the xy-plane aligns with the turntable plane. (**b**) ISAR measurement of the mock-up satellite, generated by the incoherent sum of 80 sub-apertures, each with an integration angle of 11.1°. The color bar represents the amplitude in dB. (**c**) Interferogram of the mock-up satellite measurement from (**b**) using a base length of 21 cm. The interferogram is cut to areas with $\gamma \geq 0.65$. The color bar represents the phase in degree.

This scenario was imaged using the same setup as shown above. The two-dimensional radar image can be seen in Figure 11b with the interferogram shown in Figure 11c. The interferogram is reduced to only show regions of high coherence (by applying the mask from Equation (6)), as the interferogram holds no information in regions where no echo is present in the regular image.

Taking a look at the satellite in the ISAR image, most of its features can be identified. The dish, the mock-up solar panel, and the edge struts are clearly visible. Together with the interferogram, more information can be inferred from the object. The color of the interferogram corresponds to the phase extracted at the given image pixel. As seen in Equation (4), an increase in the phase also means an increase in the height above the

focal plane, which is offset from the turntable by 44 cm. Using this knowledge, much more information can be extracted from the image. Most notably, the mock-up solar panel shows a linear gradient toward the negative y-direction. An increasing offset of the solar panel to the imaging plane can be inferred. This information is not contained in the regular image. Moreover, the extension arm at the back of the satellite can be identified with a large offset or height, respectively. But to be most clear, interferometry can only assign each pixel a single offset height. This makes it, for example, very useful for Earth observation and the creation of a digital elevation model (DEM). However, complex objects such as satellites are not well described by a surface. This is why IoSiS's ultimate goal is to move toward true three-dimensional imaging through the use of tomography.

4.3. Tomographic Measurements

Furthermore, the interferometric quasi-2D acquisition will be extended and compared to the true three-dimensional tomographic imaging. The same mock-up satellite depicted in Figure 11a was also tomographically imaged. The same radar was used to acquire the tomogram, where the antenna positions were sampled sequentially by the use of a motorized linear axis. In total, 32 antenna positions were used to span a look angle of $\vartheta \approx 11.1^\circ$ for twice the resolution in elevation as in the azimuth. To visualize the tomographic measurements, two image products can be seen in Figure 12. A common approach to visualize medical three-dimensional tomograms is a maximum intensity projection (MIP) [20]. Computing the MIP in the context of ISAR tomography can also be performed, and the MIP through the y-axis is shown in Figure 12a. This view is perpendicular to the ISAR image shown in Figure 11b and thus provides a new look at the data, which was previously not possible. The non-parallelism of the mock-up solar panel to the turntable and thus the focal plane of the interferometric case can be seen here. This feature is also revealed in the interferogram in Figure 11c. To demonstrate the superiority of true three-dimensional imaging of satellites, a different view on the tomogram can be seen in Figure 12b. Here, a cut through the tomogram is visualized through the center of the model. More precisely, a cut through the yz-plane at $x = -23\,\mathrm{cm}$ is plotted. This cut plane slices through the mock-up antenna dish and its feed point. These features are highlighted in light red in the cut image to help with the visualization. The separation of multiple scatterers along the z-axis can be seen, which is not possible through interferometric ISAR imaging.

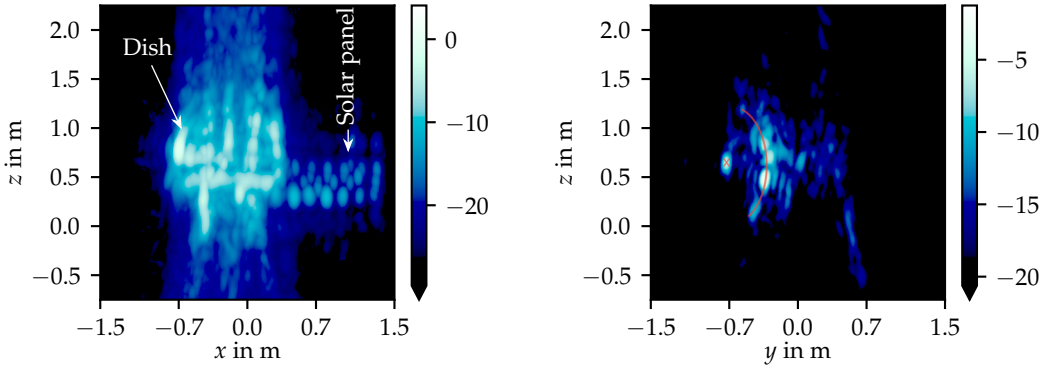

(**a**) (**b**)

Figure 12. Tomographic measurements of the mock-up satellite. The complete tomogram was created by the sum of 80 sub-apertures each with an integration angle of 11.1° in the azimuth and in elevation 32 antenna positions with an angular spacing as seen from the turntable of $\approx 0.35^\circ$. (**a**) A MIP through the y-axis of the measured tomogram. The color represents the normalized amplitude in dB. (**b**) A cut through the tomogram's zy-plane at $x = -23\,\mathrm{cm}$. The color represents the normalized amplitude in dB. To aid the interpretation, the dish parabola and its feed point are drawn in light red.

Visualizations in the form of interactive animations allow the human brain an intuitive interpretation of three-dimensional data. This can be in the form of an MIP with a changing viewpoint or a cut plane moving through the tomogram.

4.4. Comparison of Interferometric and Tomographic Measurements

To emphasize the differences in the imaging approach using a single aperture or multiple apertures, a one-to-one comparison can be made. Using the interferometric measurement from above, the same image product as the tomographic measurement can be generated. Each pixel can be evaluated to be at a specific height using information contained in the interferometric phase. Starting, then, from an empty volume, each pixel can then be put at its three-dimensional location. This results in the same image product as the tomographic measurement and can thus be visualized in the same way. A comparison can be found in Figure 13, where the true three-dimensional measurement is shown in Figure 13a and the new interferometric image product is shown in Figure 13b. It is again an MIP but now visualized in a three-dimensional way, where the MIP is performed through all native axes of the Cartesian coordinate system. Taking a first look at the tomographic acquisition, the view shown on the xy-plane closely resembles the regular ISAR image, but with an infinite focus depth as no defocussing for targets outside the focal plane occurs. On the MIPs through the other axes, the mock-up satellite can be clearly seen. For example, the feed point of the mock-up antenna dish stands out in both projections on the xy- and yz-plane.

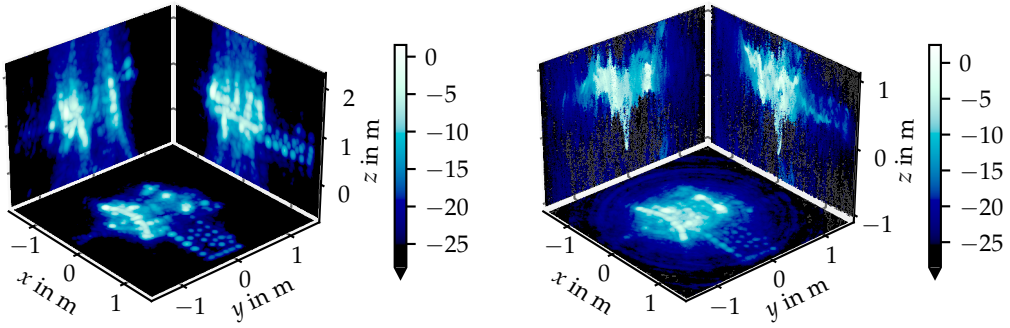

(**a**) (**b**)

Figure 13. Comparison of a tomographic measurement of the mock-up satellite with an identical image product generated by an interferometric measurement. (**a**) An MIP through all axes of the measured tomogram. The color represents the normalized amplitude in dB. (**b**) An MIP through all axes of the volumetric projection of the interferometric measurement. The color represents the normalized amplitude in dB.

Taking a look at the interferometric measurements, the interpretation of the images is far more challenging. The regular ISAR image is projected on the xy-plane. As interferometry cannot split multiple scatterers along the normal direction of the imaging plane, no clear three-dimensonal visualization can be achieved. While the round shape of the mock-up dish can be well identified in the tomographic case, only the phase superposition can be seen in the interferometric measurement. However, the mock-up solar panel can be seen in its place in space. Looking at the image placed at the xz-plane, on the right-hand side, the tilted solar panel can be identified. The visualization is not as clear as in the tomographic case because the phase relationship of the point spread function (PSF) extends the imaged scatterers on the z-axis. To conclude the comparison, complex objects are not well described by a topography, which is what interferometric measurement products deliver. There may exist further interferometric image products, which allow more insight into the data. The fundamental limitations, however, cannot be overcome using only a single secondary receiver.

4.5. Change Detection

In conclusion, an exemplary application for IoSiS, comprising an initial test of change detection based on tomographic acquisition, will be presented. This will provide satellite operators with a new tool to identify changes caused by external factors, such as the impact of space debris. Change detection in the field of SAR with respect to Earth observation is not new, and many complex methods for detecting changes have already been proposed, e.g., [21]. In the context of space surveillance and imaging of satellites in space, this is a new frontier requiring new research. The in situ detection of changes will be a valuable tool for satellite operators. In order to illustrate this methodology, the most elementary approach to discerning changes, an incoherent difference, is presented here. This methodology is founded upon tomographic imaging, wherein a comprehensive volume is observed. Two tomograms, $s_1(x,y,z)$ and $s_2(x,y,z)$ are, taken at different instances in time, and the incoherent difference tomogram can be created by Equation (11). A prior amplitude alignment on strong persistent scatters is mandatory to achieve a good difference estimation.

$$\Delta s(x,y,z) = |s_2(x,y,z)| - |s_1(x,y,z)| \tag{11}$$

As can be seen in Figure 14a, some modifications were made to the satellite.The satellite model was then observed both prior to and after the introduced changes. To demonstrate the capability to detect changes and localize them in all three spatial dimensions, a cut plane was put through the change tomogram and is shown in Figure 14b.

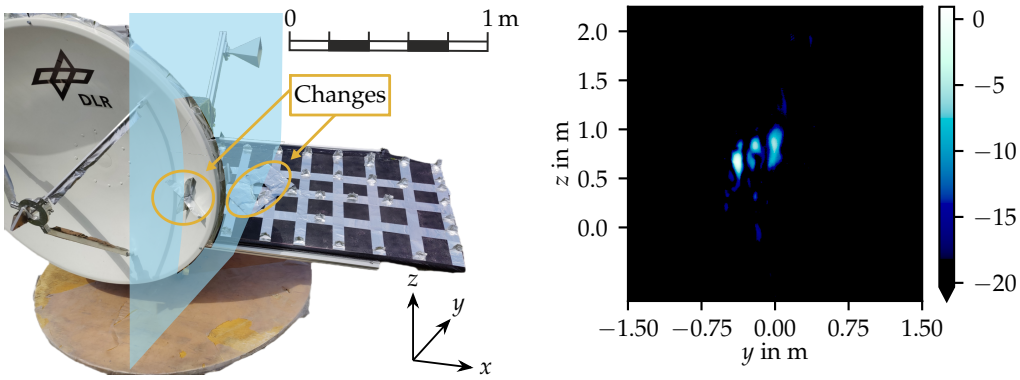

(**a**) (**b**)

Figure 14. Tomographic measurement setup and measurement results for change detection as a conceptional tool using the built radar demonstrator. (**a**) Photographic image of the mock-up satellite with the intentional changes; the z-axis of the coordinate system aligns with the axis of rotation of the turntable, and the xy-plane aligns with the turntable plane. (**b**) A cut through the incoherent difference tomogram. The cut plane is visualized in (**a**); the color represents the normalized amplitude in dB.

5. Conclusions

The work presented here allows insights into the interferometric as well as tomographic imaging of satellites and is a necessary groundwork for expanding radar space surveillance systems into new frontiers for the three-dimensional imaging of satellites in space.

The superiority of three-dimensional acquisitions compared to regular 2D images can be clearly seen here. The ability to image complex objects such as satellites in three dimensions is of particular benefit in this context. Interferometric measurements are well suited to observe the height topography of a surface object, but in the context of imaging space objects, this is only partly sufficient. The ground-based measurement results shown here, giving confidence in first interferometric measurements for a quasi-three-dimensional observation for satellites.

The extension of IoSiS toward a full tomographic system requires a substantial hardware expenditure as the number of receivers needed is on the order of 100. Moreover, an optimized receiver array with regard to the orbit geometry and the use of compressed sensing will be investigated in the future. In terms of technology, the radar of IoSiS will be enhanced in regard to its current timing capability using the new FPGA unit shown here. The interfaces to implement more receivers into IoSiS are currently set up. Of particular importance is the research currently being conducted into new synchronization techniques for coherent multistatic operation.

It would be reasonable to posit that the logical next step is to gradually move IoSiS toward full tomographic imaging capability by sequentially adding receivers. Each added baseline will bring valuable information. This will facilitate the acquisition of additional information, commencing with the newly available capability for interferometry.

Author Contributions: Conceptualization, S.A. and M.P.; methodology, F.H.; software, F.H.; validation, M.J., S.A. and M.P.; formal analysis, F.H.; investigation, F.H.; resources, M.J., S.A. and M.P.; writing—original draft preparation, F.H.; writing—review and editing, M.J., S.A. and M.P.; visualization, F.H.; supervision, M.J., S.A. and M.P.; project administration, M.P. All authors have read and agreed to the published version of the manuscript.

Funding: This research received no external funding.

Data Availability Statement: Dataset available on request from the authors.

Conflicts of Interest: The authors declare no conflicts of interest.

Abbreviations

The following abbreviations are used in this manuscript:

DLR	German Aerospace Center
DEM	Digital elevation model
FPGA	Field-programmable gate array
IoSiS	Imaging of Satellites in Space
ISAR	Inverse synthetic aperture radar
LO	Local oscillator
MIP	Maximum intensity projection
PSF	Point spread function
RX	Receiver
SAR	Synthetic aperture radar
SSA	Space situational awareness
SSD	Solid-state drive
TX	Transmitter

References

1. Anger, S.; Jirousek, M.; Dill, S.; Kempf, T.; Peichl, M. High-Resolution Inverse Synthetic Aperture Radar Imaging of Satellites in Space. *IET Radar Sonar Navig.* **2024**, *18*, 544–563. [CrossRef]
2. Hamad, A.; Berens, P. High Resolution 3D ISAR Image Formation via Interferometry Combined with Multi-Look Processing of Wide Angle Data. In Proceedings of the EUSAR 2024, 15th European Conference on Synthetic Aperture Radar, Munich, Germany, 23–26 April 2024; pp. 629–632.
3. Thindlu Rudrappa, M.; Albrecht, M.; Knott, P. Characterisation of Resident Space Objects Using Multistatic Interferometric Inverse Synthetic Aperture Radar Imaging. *IET Radar Sonar Navig.* **2024**, *18*, 620–634. [CrossRef]
4. Soumekh, M. *Synthetic Aperture Radar Signal Processing with MATLAB Algorithms*; J. Wiley: New York, NY, USA, 1999.
5. Bocker, R.P.; Jones, S.A. ISAR Motion Compensation Using the Burst Derivative Measure as a Focal Quality Indicator. *Int. J. Imaging Syst. Technol.* **1992**, *4*, 285–297. [CrossRef]
6. Yang, J.; Wang, Y. Three-Dimensional Interferometric Inverse Synthetic Aperture Radar Imaging of Ship Target Based on Cubic Phase Signal Model. *IET Radar Sonar Navig.* **2024**, *18*, 1691–1709. [CrossRef]
7. Bocker, R.P.; Henderson, T.B.; Jones, S.A.; Frieden, B.R. New Inverse Synthetic Aperture Radar Algorithm for Translational Motion Compensation. In Proceedings of the Stochastic and Neural Methods in Signal Processing, Image Processing, and Computer Vision, San Diego, CA, USA, 24–26 July 1991; Chen, S.S., Ed.; SPIE: Bellingham, WA, USA, 1991; pp. 298–310. [CrossRef]
8. Bamler, R.; Hartl, P. Synthetic Aperture Radar Interferometry. *Inverse Probl.* **1998**, *14*, R1. [CrossRef]

9. Yu, H.; Lan, Y.; Yuan, Z.; Xu, J.; Lee, H. Phase Unwrapping in InSAR : A Review. *IEEE Geosci. Remote Sens. Mag.* **2019**, *7*, 40–58. [CrossRef]
10. Gini, F.; Lombardini, F.; Montanari, M. Layover Solution in Multibaseline SAR Interferometry. *IEEE Trans. Aerosp. Electron. Syst.* **2002**, *38*, 1344–1356. [CrossRef]
11. Kempf, T.; Anglberger, H.; Suess, H. Depth-of-Focus Issues on Spaceborne Very High Resolution SAR. In Proceedings of the 2012 IEEE International Geoscience and Remote Sensing Symposium, Munich, Germany, 22–27 July 2012; pp. 7448–7451. [CrossRef]
12. Hochberg, F.; Jirousek, M.; Anger, S.; Peichl, M. Tomographic ISAR Imaging of Satellites: A Ground-Based Experimental Validation. In Proceedings of the 2024 Kleinheubach Conference, Miltenberg, Germany, 24–26 September 2024; pp. 1–4. [CrossRef]
13. Werninghaus, R.; Buckreuss, S. The TerraSAR-X Mission and System Design. *IEEE Trans. Geosci. Remote Sens.* **2010**, *48*, 606–614. [CrossRef]
14. NASA. International Space Station Facts and Figures. 16 July 2024. Available online: https://www.nasa.gov/feature/facts-and-figures (accessed on 28 August 2024).
15. UCS Satellite Database. 1 May 2023. Available online: https://www.ucsusa.org/resources/satellite-database (accessed on 28 August 2024).
16. Griffiths, H.D. High Resolution Radar Cross-Section Imaging. L. Mensa Dean, 270 Pp. 23·5 × 15·5 cm, Artech House, Boston and London 1991. £50. *J. Navig.* **1991**, *44*, 444–445. [CrossRef]
17. Zhu, X.X.; Bamler, R. Tomographic SAR Inversion by L_1-Norm Regularization—The Compressive Sensing Approach. *IEEE Trans. Geosci. Remote Sens.* **2010**, *48*, 3839–3846. [CrossRef]
18. Rohling, H. Radar CFAR Thresholding in Clutter and Multiple Target Situations. *IEEE Trans. Aerosp. Electron. Syst.* **1983**, *AES-19*, 608–621. [CrossRef]
19. Harris, J. On the Use of Windows for Harmonic Analysis with the Discrete Fourier Transform. *IEEE Proc.* **1978**, *66*, 51–83. [CrossRef]
20. Wallis, J.; Miller, T.; Lerner, C.; Kleerup, E. Three-Dimensional Display in Nuclear Medicine. *IEEE Trans. Med. Imaging* **1989**, *8*, 230–297. [CrossRef]
21. Méndez Domínguez, E.; Magnard, C.; Meier, E.; Small, D.; Schaepman, M.E.; Henke, D. A Back-Projection Tomographic Framework for VHR SAR Image Change Detection. *IEEE Trans. Geosci. Remote Sens.* **2019**, *57*, 4470–4484. [CrossRef]